Available online at www.sciencedirect.com
ScienceDirect
Journal of the European Ceramic Society 28 (2008) 1961–1971
www.elsevier.com/locate/jeurceramsoc

Fracture behaviour of microcrack-free alumina–aluminium titanate ceramics with second phase nanoparticles at alumina grain boundaries

S. Bueno [a], M.H. Berger [b], R. Moreno [a], C. Baudín [a,*]

[a] *Instituto de Cerámica y Vidrio (CSIC). C. Kelsen 5, 28049 Madrid, Spain*
[b] *Ecole des Mines de Paris, Centre des Matériaux, 91003 Evry Cedex, France*

Received 12 October 2007; received in revised form 19 December 2007; accepted 4 January 2008
Available online 4 March 2008

Abstract

Alumina + 10 vol.% aluminium titanate composites were obtained by colloidal filtration and reaction sintering of alumina and titania. The materials were dense with aluminium titanate grains of average sizes 2.2–2.4 μm located mainly at alumina triple points. The reaction sintering schedule promoted the formation of additional nanometric grains, identified as aluminium titanate using STEM–EDX analysis between the alumina grains. This special microstructure led to a change of the toughening mechanism from the typical crack bridging reported for microcrack-free composites fabricated from alumina and aluminium titanate powders to microcracking.

The identification of microcracking as the main toughening mechanism was done from the analysis of stable fracture tests of SENVB samples in three points bending and fractographic observations. Monophase alumina materials with similar grain sizes were used as reference.

Different fracture toughness parameters were derived from the load–displacement curves: the critical stress intensity factor, K_{IC}, the critical energy release rate, G_{IC}, the J-Integral and the work of fracture, γ_{WOF}, and the R curves were also built. The comparison between the linear elastic fracture parameters and the non-linear ones revealed significant toughening and flaw tolerance.

Keywords: D. Al_2O_3; D. Al_2TiO_5; C. Mechanical properties; C. Toughening; B. Nanocomposites

1. Introduction

The use of ceramic materials in structural applications is limited by the "flaw sensitive" fracture, occurring spontaneously from natural flaws, inherent to the brittle behaviour. The "flaw tolerance" approach deals with the development of microstructures that originate toughening mechanisms to reduce the sensitivity of the strength to the size of any processing or induced flaw, thus improving the reliability of the materials.[1–3] Such mechanisms originate an increasing resistance with continued crack extension, rising *R*-curve behaviour, and most of them are caused by localized internal residual stresses in the materials.

Alumina (Al_2O_3)–aluminium titanate (Al_2TiO_5) materials can offer improved flaw tolerance and toughness.[4–12] Thermal expansion of aluminium titanate is highly anisotropic ($\alpha_{a25-1000\,^\circ C} = 10.9 \times 10^{-6}\,^\circ C^{-1}$, $\alpha_{b25-1000\,^\circ C} = 20.5 \times 10^{-6}\,^\circ C^{-1}$, $\alpha_{c25-1000\,^\circ C} = -2.7 \times 10^{-6}\,^\circ C^{-1}$)[1] [13] and alumina shows limited anisotropy ($\alpha_{a25-1000\,^\circ C} = 8.4 \times 10^{-6}\,^\circ C^{-1}$, $\alpha_{c25-1000\,^\circ C} = 9.2 \times 10^{-6}\,^\circ C^{-1}$),[14] thus, high tensile or compressive stresses, depending on the particular crystallographic orientation of the grains, would develop during cooling from the sintering temperature at the grain–matrix interfaces due to thermal expansion mismatch. Depending on grain size and the characteristics of the grain boundaries, microcracking might occur during cooling from sintering and/or during fracture.

In the early 90s alumina–aluminium titanate composites with aluminium titanate contents 20–30 vol.% obtained from alumina and aluminium titanate mixtures, were studied by other authors.[4–7] Crack bridging by second phase agglomerates and by large alumina grains was identified as the toughening mechanism leading to *R*-curve behaviour, assessed by the indentation–strength method; no toughness values were

* Corresponding author. Tel.: +34 91 7355840; fax: +34 91 7355843.
E-mail address: cbaudin@icv.csic.es (C. Baudín).

[1] In this work, β-Al_2TiO_5 orthorhombic crystal is described by a b-face centered unit cell, space group *Bbmm*, $a = 9.439$ Å, $b = 9.647$ Å, $c = 3.593$ Å.

0955-2219/$ – see front matter © 2008 Elsevier Ltd. All rights reserved.
doi:10.1016/j.jeurceramsoc.2008.01.017

provided for the fine-grained materials with homogeneous microstructures. All materials presented different levels of microcracks in the "as sintered" state. A latter work on microcrack-free and fine-grained alumina + 10 vol.% aluminium titanate fabricated from alumina and aluminium titanate mixtures showed that second phase grains as well as matrix grains could act as bridges in the wake of the propagating crack.[8] This material presented increased thermal shock resistance than a monophase alumina of similar grain size while maintaining strength.

The initial objective of this work was to investigate the possibilities of crack bridging in fine-grained, homogeneous and microcrack-free alumina–10 vol.% aluminium titanate composites for flaw tolerance. Reaction sintering of alumina and titania was used as processing route. [15] The microstructures of the reaction sintered materials were different than that of the previously studied material, with a bimodal distribution of aluminium titanate grains with nanoparticles located at the alumina grain boundaries. The characterization of the fracture process in the composites and monophase alumina materials, combining different fracture parameters together with fractographic observations, has allowed determining the extreme effect of the grain boundary characteristics in the fracture process. The major toughening mechanism identified in the composite studied here has been microcracking.

2. Quantification of fracture toughness

In general, the linear elastic fracture behaviour of ceramic materials is quantified by the following toughness parameters: critical stress intensity factor in mode I, K_{IC}, and critical strain energy release rate, G_{IC}. For three-point-bend beams, the values of K_{IC} can be determined from the notch depths and the maximum loads reached in the tests according to the general stress intensity formulation, valid for any notch depth, a, in linear elastic materials (Eq. (1))[16]:

$$K_I = \frac{3PL}{2BW^{3/2}} \times Y(\alpha) \quad (1)$$

where P is the maximum load, L is the span, B and W are the width and the thickness of the bars, α is the normalized notch length ($\alpha = a/W$) and $Y(\alpha)$ is a shape function depending on the span to thickness ratio (L/W, Eq. (2)).

$$Y(\alpha) = \frac{\sqrt{\alpha}(1.99 + 0.83\alpha - 0.31\alpha^2 + 0.14\alpha^3 + 4(W/L) \times(-0.09 - 0.42\alpha + 0.82\alpha^2 - 0.31\alpha^3))}{(1-\alpha)^{3/2} \times (1 + 3\alpha)} \quad (2)$$

From K_{IC} and Young's modulus, G_{IC} can be calculated according to the analysis of Irwin that relates the stress-derived fracture toughness (K_{IC}) and the energy-derived fracture toughness (G_{IC}) for plane strain conditions (Eq. (3)):

$$G_{IC} = \frac{K_{IC}^2}{E'} \quad (3)$$

where $E' = E/(1-\nu^2)$ is the generalized Young's modulus for plane strain (E is the Young's modulus and ν is the Poisson's ratio).

The activation of toughening mechanisms during the fracture of ceramic materials gives rise to inelastic strain processes that produce additional release of the elastic energy accumulated in the material at the moment of fracture initiation and/or contributing to the retardation of crack growth.[17] The inelastic strain levels achieved in ceramic materials can be enough to restrict the direct utilization of linear elastic fracture toughness parameters since they become dependent on testing and specimen geometry for non-linear materials.[18–20]

The rising R-curve behaviour, increasing K_{IC} or G_{IC} with crack extension (Δa), has traditionally been the most utilized approach to analyze deviations from the linear behaviour induced by toughening in dense and fine-grained ceramics.[19,21–22] In equilibrium conditions, the applied stress intensity factor, K_I, is balanced by the crack growth resistance, K_R, and maximum values of this latter, K_∞, are reached when the process zone is completely developed.

In order to build the R curve of the materials, crack growth resistance and crack length values during crack extension are needed. The "in situ" measurement of crack length can be a problem especially for materials such as alumina–aluminium titanate composites, constituted by phases with large differences in hardness and in which residual stresses are present. The low quality of polished surfaces of relatively large specimens (e.g.: bending bars with lateral face dimension 50 mm × 6 mm) of such materials makes the identification and monitoring of the propagating crack enormously difficult.

Alternatively, the R curves can be determined by the indirect method that defines an equivalent crack length as a function of the elastic compliance of the specimen, C.[23–25] For parallelepiped bars with straight through notches tested in three points bending, the expression provided by Guinea et al.[16] can be utilized (Eq. (4)):

$$\alpha = \frac{(CE'B)^{1/2}}{[CE'B + q_1(CE'B)^{1/2} + q_2(CE'B)^{1/3} + q_3]^{1/2}} \quad (4)$$

where E', α and B have the same meaning as before (Eq. (1)) and q_i ($i = 1, 2, 3$) are parameters that depend on the L/W ratio ($2.5 \le (L/W) \le 16$).

In a lesser extent, the non-linear fracture toughness parameter J-integral and work of fracture, γ_{WOF}, have been used by Li and co-workers,[26] Bradt and co-workers[27] and Sakai et al.[18] to characterize ceramic materials with coarser microstructures and higher levels of non-linearity such as refractories and fiber reinforced ceramic matrix composites.

The J-integral is an energy term that generalizes the energy release rate, G, to include non-linear elastic and inelastic behaviours and that describes the total energy of the crack-tip stress–strain field.[28] The critical value, J_{IC}, constitutes a fracture criterion for materials where the toughening occurs along limited crack propagation such as those that present small bridging zones.[29]

There are two main different procedures to determine J_{IC},[26–27,30] either based on the determination of the energy absorbed by the specimen, given by the area under the corresponding load–crack opening displacement curve,[30] or from load–displacement curves by conducting tests on two specimens with different crack lengths.[26] Both methods require the identification of the propagating crack. In this work, a graphical procedure was used[27] in which J_{IC} is calculated (Eq. (5)) from the difference between the areas under the load (P)–displacement (δ) curves of the notched non-linear specimens (A_I) and an unnotched linear elastic specimen of the same material (A_E) for equal maximum loads (P_{max}):

$$J_{IC} = \frac{2}{(W-a)B} \times \int_0^{\delta_{max}} P\mathrm{d}\delta = \frac{2}{(W-a)B} \times (A_I - A_E) \quad (5)$$

where a, W and B have the same meaning as before (Eq. (1)).

The work of fracture is defined as the mean energy consumption required forming the unit fracture surface area and the additional process zone. It accounts an average value of the whole fracture process that does not require any assumption on the constitutive equation of the cracked body to deal with crack growth problems as discussed by Sakai et al.[18] The work of fracture is obtained by dividing the work done on the specimen to propagate the crack, given by the area under the load–displacement curves, by the area of the newly created surfaces. For parallelepiped bars with straight through notches tested in flexure, this area is twice the area of the unnotched part of the cross-section of the specimens.

3. Experimental procedure

Monoliths of monophase alumina (A) and alumina + 10 vol.% aluminium titanate (A10) composites were manufactured by colloidal filtration from aqueous alumina, Al_2O_3, and titania, TiO_2, suspensions using the optimum green processing conditions previously established.[15,31] A mixture of alumina (≅95 wt.%) and titania (≅5 wt.%) was used to obtain the sintered composition with 10 vol.% of aluminium titanate, Al_2TiO_5. The starting materials were commercial α-Al_2O_3 (Condea, HPA05, USA) and TiO_2-anatase (Merck, 808, Germany) powders. The powders were dispersed in deionised water by adding 0.5 wt.% (on a dry solids basis) of a carbonic acid-based polyelectrolyte (Dolapix CE64, Zschimmer-Schwarz, Germany). Suspensions were prepared to a solids loading of 50 vol.% and ball milled with alumina jar and balls during 4 h.

Plates of the materials with 70 mm × 70 mm × 10 mm dimensions were obtained by slip casting, removed from the moulds and dried in air at room temperature for at least 24 h. Sintering of the green plates was performed in air in an electrical box furnace (Termiber, Spain) at heating and cooling rates of 2 °C min^{-1}, with 4 h, dwell at 1200 °C during heating and two different treatments at the maximum temperature: 2 h, dwell at 1450 °C and 3 h, dwell at 1550 °C. For all tests, samples were diamond machined from the sintered blocks.

Densities of the sintered compacts were determined by the Archimedes's method in water (European Standard EN 1389:2003) and relative densities were calculated from these values and those of theoretical densities calculated taking values of 3.99 g cm^{-3} for alumina (ASTM 42-1468) and 3.70 g cm^{-3} for aluminium titanate (ASTM 26-0040).

Microstructural characterization on polished and thermally etched (20 °C below the sintering temperature during 1 min) surfaces was performed by field emission gun scanning electron microscopy (FEG-SEM, Hitachi, S-4700, Japan). The true average grain size was determined by the linear intercept method considering at least 200 grains for each phase and using the correction factor $4/\pi$.[32] Chemical profiles across grain boundaries were achieved by STEM–EDX (energy dispersed X-ray spectroscopy, coupled with scanning transmission electron microscopy, Tecnai F20-ST, The Netherlands) at 200 kV. Thin foils were prepared by mechanical polishing of a 3 mm diameter disk up to 15 μm in thickness followed by Ar^+ milling (PIPS Gatan, USA, operating at 5 kV with a beam incidence of 6%).

Bars of 25 mm × 2 mm × 2.5 mm were diamond machined from the sintered blocks for bend strength tests (three points, 20 mm span, 0.5 mm min^{-1}; Microtest, Spain). Engineering stress–strain curves were calculated from the load values and the displacement of the central part of the samples recorded during the bending tests and static Young's modulus was determined from the initial linear part of the curves. Given results for strength and static Young's modulus are the average of five determinations and the standard deviation.

Strength was also determined for specimens of a previously studied A10 composite[8] (named A10AT) fabricated from powders of Al_2O_3 (90 vol.%) and Al_2TiO_5 (10 vol.%) obtained by reaction of Al_2O_3 and TiO_2 powders[33] and sintered at 1500 °C; the starting Al_2O_3 and TiO_2 powders used were the same as in this work.

Single-Edge-V-Notch-Beams (SEVNB) of 4 mm × 6 mm × 50 mm were tested in a three points bending device using a span of 40 mm and a cross-head speed of 0.005 mm min^{-1} (Microtest, Spain). The compliance of the whole testing system (machine, supports, load cell and fixtures) was determined by testing a thick (25 mm × 25 mm × 100 mm) unnotched alumina bar. The obtained value was 1.5×10^{-7} m/N. The notches were initially cut with a 150 μm wide diamond wheel. Using this slot as a guide, the remaining part of the notch was done with a razor blade sprinkled with diamond pastes of successively 6 and 1 μm. Three relative notch depths, α, with approximately 0.4, 0.5 and 0.6 of the thickness of the samples (W) were tested. The tip radii of all notches were determined from optical observations and they were always found to be below 20 μm. The curves load–displacement of the cross-head of the load frame were recorded. All curves were corrected by subtracting the compliance of the testing set up.

Additional tests were performed with unnotched specimens up to loads (≅20 N) well below the starting of the non-linear behaviour and the obtained values of stiffness were used to calculate J_{IC} following the procedure described above (Eq. (5)).

The fracture toughness parameters, i.e., critical stress intensity factor, K_{IC}, critical strain energy release rate, G_{IC}, critical J-integral, J_{IC}, and work of fracture, γ_{WOF}, were calculated from the curves obtained during the SEVNB tests for the three

Table 1
Properties of the materials: average grain size (G), relative density (ρ), static Young's modulus (E) and three points bending strength (σ_f)

	G_A (S.D.) (μm)	G_{AT} (S.D.) (μm)	ρ (S.D.) (% theoretical)	E (S.D.) (GPa)	σ_f (S.D.) (MPa)
A-1450	3.5 (0.3)	–	98.1 (0.3)	379 (8)	456 (29)
A-1550	5.5 (0.6)	–	98.1 (0.5)	376 (6)	349 (31)
A10-1450	3.2 (0.4)	2.2 (0.1)	97.3 (0.5)	301 (4)	261 (6)
A10-1550	3.9 (0.3)	2.4 (0.2)	97.2 (0.3)	272 (10)	230 (1)
A10AT			98.5 (0.1)	367 (5)	360 (31)

A: alumina, AT: aluminum titanate; S.D.: standard deviation.

notch depths utilized. Reported values are the average of three determinations and errors are the standard deviations. R curves were determined from the load versus displacement curves corresponding to tests performed with a relative notch depth of 0.6 of the thickness of the samples.

The fracture surfaces of tested strength and SEVNB specimens were characterized by FEG-SEM. Also small samples of the lateral faces (face dimension 50 mm × 6 mm) containing the notches and the cracks were polished and chemically etched (HF-10 vol.%–3 min) in order to observe the zones surrounding the propagating cracks to characterize the process zones. In order to complement the fractographic observations, polished surfaces of composite samples indented with a Vickers point using 50 N during 10 s, were also observed.

4. Results and discussion

4.1. Microstructure

The microstructures of both aluminas were typical of materials fabricated from high-purity submicron alumina powders. The material sintered at 1450 °C was constituted by equidimensional grains with a narrow distribution of relatively small sizes whereas that sintered at 1550 °C presented a coarser microstructure with a wide distribution of sizes and pore trapping associated with exaggerated grain growth. The microstructural parameters together with the density, static Young's modulus and strength values are reported in Table 1.

The composites presented micrometer sized (2.2–2.4 μm, Fig. 1a and b, Table 1) aluminium titanate grains homogeneously distributed and located mainly at alumina triple points and grain boundaries and alumina grains of sizes similar to those of the monophase alumina sintered at 1450 °C (3.2–3.9 μm, Fig. 1a, Table 1). Submicrometric second phase grains were also observed inside the alumina grains and occasionally at grain boundaries (Fig. 1a). Additional nanometer sized grains were observed at grain boundaries by SEM (Fig. 1b).

In Fig. 2 characteristic STEM observations for the composites sintered at 1550 °C together with EDX chemical analysis are shown. The ratios (wt.%) Al/O (≅1.4) and Ti/O (≅1.3) in the grains of aluminium titanate (Fig. 2a) were always well higher than those corresponding to the stoichiometric, 0.68 and 0.60, respectively. The $K_{\alpha,\beta}$ radiations emitted by light elements have lower energies and are preferentially absorbed by carbon contamination formed during the spot analyses. This induces an underestimation of oxygen concentration. Also, the ratio Ti/Al (0.85–0.87) was slightly lower than the stoichiometric (0.89). Nevertheless, results of these semi quantitative analyses are valid for comparative purposes. No Ti was detected inside the alumina grains of the composites (Fig. 2a), whose analyses were simi-

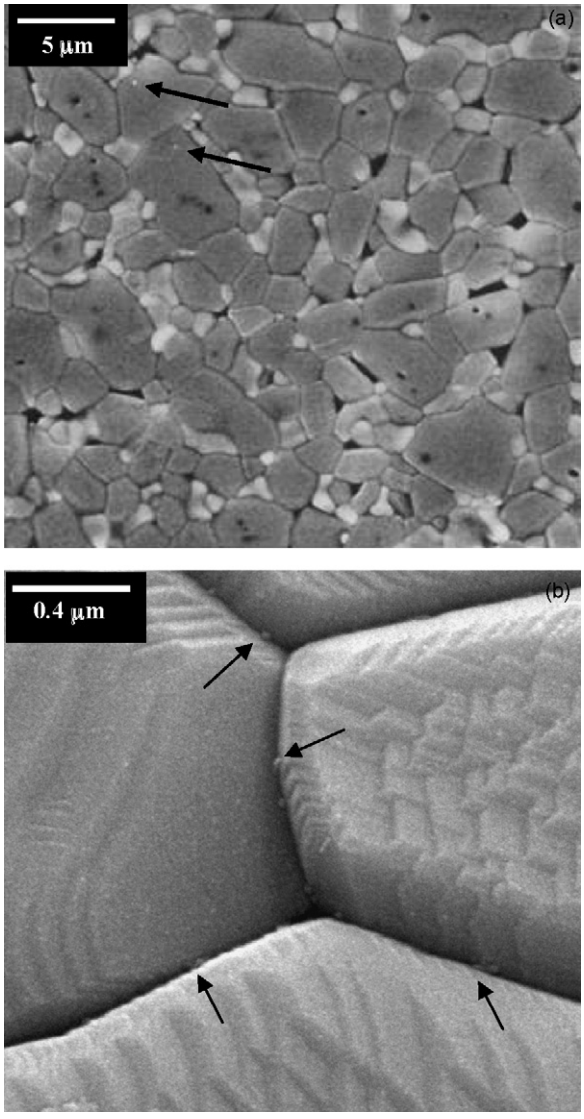

Fig. 1. Characteristic microstructures of the studied A10 composites. Scanning electron micrographs of polished and thermally etched surfaces. Alumina grains appear with dark grey colour whereas micrometer sized aluminium titanate grains have lighter gray shade. (a) Composite A10 sintered at 1450 °C. Submicrometric second phase grains inside the alumina matrix are pointed by arrows. (b) Composite A10 sintered at 1550 °C. Detail of nanosized (arrows) aluminium titanate grains located at the boundaries between the alumina grains.

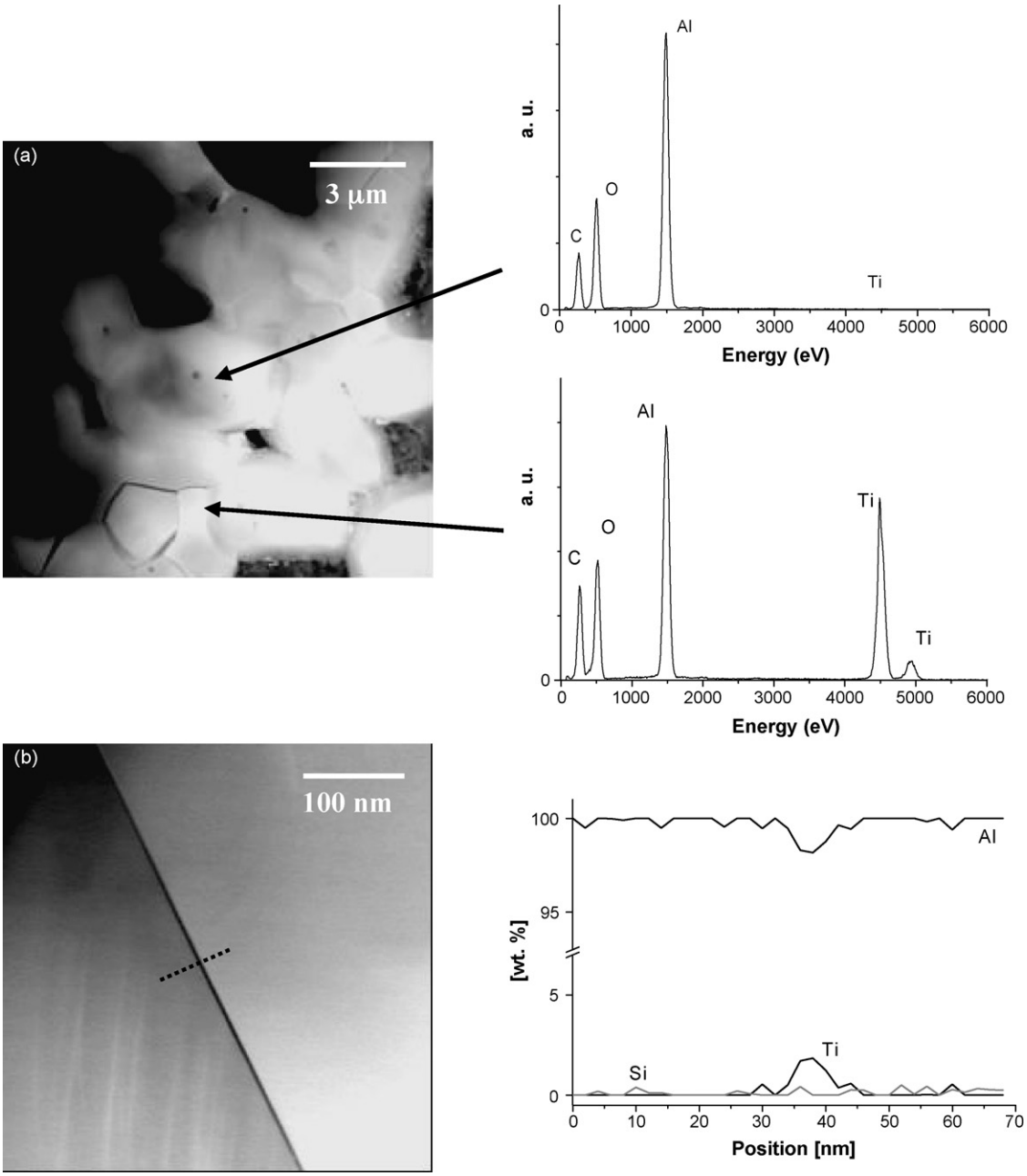

Fig. 2. Characteristic scanning transmission electron microscopy (STEM) observations for the A10 composites sintered at 1550 °C together with EDX chemical analysis (a.u. = arbitrary units). (a) Alumina and aluminium titanate grains. No Ti was detected inside the alumina grains. (b) Chemical profile along a line traversing an alumina/alumina grain boundary showing enrichment in Ti. Negligible Si contents are detected.

lar to those of the monophase specimens. However, the EDX line profiles across alumina grain boundaries in the composites (Fig. 2b) showed a systematic evidence of Ti segregation at the alumina/alumina grain boundaries. Values from 0.5 to 2.5 Ti wt.% were detected with no systematic variation with alumina grain size.

The presence of the major impurity in the starting powders, Si, was also investigated and only no Si or negligible Si contents were found in the grain boundaries (Fig. 2b). Moreover, STEM–EDX analysis evidenced diffusion of titanium ions across the alumina grain boundaries during sintering. Thus, the composition of the nanosized particles found by SEM (Fig. 1b) should be aluminium titanate, formed by reaction of the thermodynamically incompatible compounds alumina and titania. The fact that such particles were not observed by STEM should be due to the relatively small portions of material characterized by this method (two samples were observed).

4.2. Toughness parameters

The load–displacement curves for both composites and for the three relative notch sizes showed stable fracture. In Fig. 3 characteristic curves for specimens with a relative notch length $a/W = 0.5$ are shown. Controlled fracture was difficult to achieve

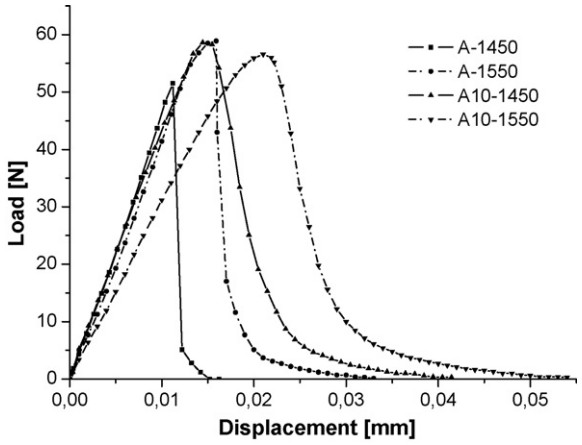

Fig. 3. Characteristic load–displacement curves recorded during the SENVB bending tests. Specimens tested with an initial relative notch length $a/W = 0.5$. Stable fracture is observed for both composites and semi-stable fracture is observed for both aluminas.

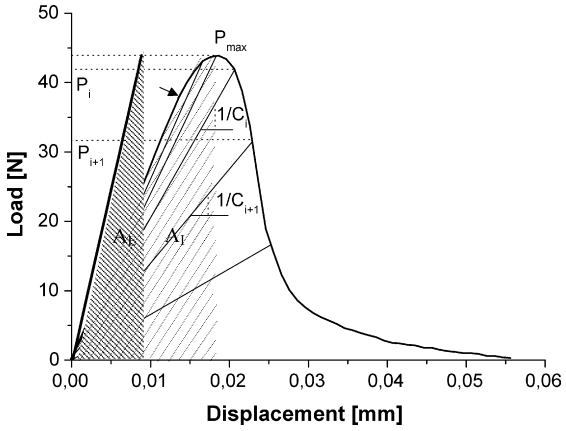

Fig. 4. Schematic representation of the procedure followed for *R*-curve determination and J_{IC} calculation.[27] The curve correspond to the A10 composite sintered at 1550 °C and tested with a relative notch depth $a/W = 0.6$. For *R*-curve determination, the arrow marks the point where the non-linear behaviour starts, selected as the onset of crack propagation. From this point, the increments in the crack length ($\Delta a = a_{i+1} - a_i$) would produce the changes in the compliance (C_i, C_{i+1}). For J_{IC} calculation (Eq. (5)), the areas under the curves corresponding to specimen tested with the notch (A_I) and to an unnotched specimen (A_E) are shown.

for the monophase alumina specimens and only semi-stable fracture was obtained for a limited number of tests of specimens with relative notch depths of 0.5 (Fig. 3). The introduction of larger notches led to the failure of the specimens during machining.

The fracture toughness parameters are summarized in Table 2. K_{IC} values were calculated using Eq. (1) and the values of the maximum loads attained during the tests and G_{IC} was calculated according to Eq. (3) from K_{IC} values and Young's modulus (E, Table 1) and using the Poisson ratio of dense and fine-grained alumina ($\nu = 0.22$).

In order to determine the increments in crack length ($\Delta a = a_{i+1} - a_i$) to build the *R* curves, the common criterion relating the onset of crack propagation in the load–displacement curves with the point where the non-linear behaviour starts (arrow in Fig. 4)[18,24,34] was used. From this point, the increments in crack length ($\Delta a = a_{i+1} - a_i$) would produce the changes in the compliance (C_i, C_{i+1}, Fig. 4). An example of the graphics used to calculate J_{IC} is depicted in Fig. 4.

For the monophase materials, the K_{IC} values were lower than those reported for aluminas with similar grain sizes ($K_{IC} \cong 3.5$–$4.5\ \text{MPa m}^{1/2}$), determined from unstable tests[35–37] and, in some cases, using specimens with notch radii larger than those utilized in this work,[36] and similar to those determined by Sbaizero et al.[38] ($K_{IC} \cong 3\ \text{MPa m}^{1/2}$) for hot-pressed aluminas using stable fracture tests. As discussed by Bar-On et al.,[39] unstable crack extension results in apparent increases of fracture toughness values compared to those determined during quasi-static crack growth. Therefore, the semi-stable crack propagation obtained in this work for the alumina specimens (Fig. 3) would give values closer to the actual fracture toughness.

Table 2
Fracture toughness parameters of the materials: critical stress intensity factor (K_{IC}), critical energy releasing rate (G_{IC}), critical J-integral (J_{IC}) and work of fracture (γ_{WOF})

	K_{IC} (S.D.) MPa m$^{1/2}$	G_{IC} (S.D.) (J/m^2)	J_{IC} (S.D.) (J/m^2)	J_{IC}/G_{IC} (S.D.)	γ_{WOF} (S.D.) (J/m^2)
A-1450					
0.5	2.9	20.4	19.2	1.0	10.5[a]
	2.8	19.6	18.9	1.0	9.8[a]
A-1550					
0.5	3.2 (0.1)	26.2 (0.7)	29.9 (3.0)	1.1 (0.1)	20.1 (2.0)[a]
A10-1450					
0.4	3.5 (0.1)	38.4 (0.8)	42.1 (3.7)	1.1 (0.1)	34.7 (1.3)
0.5	3.5 (0.2)	39.2 (0.6)	38.6 (2.9)	1.1 (0.1)	33.4 (2.3)
0.6	3.5 (0.1)	37.6 (1.2)	45.9 (3.3)	1.2 (0.1)	35.1 (1.7)
A10-1550					
0.4	3.3 (0.1)	38.4 (1.2)	50.8 (6.0)	1.3 (0.2)	40.6 (1.2)
0.5	3.3 (0.1)	37.4 (2.6)	55.4 (4.1)	1.5 (0.1)	41.9 (3.0)
0.6	3.3 (0.2)	37.9 (2.0)	53.1 (2.3)	1.4 (0.1)	39.6 (2.1)

S.D.: standard deviation. For monophase alumina materials valid tests were obtained only with a relative notch depth of 0.5. The values of the two tests obtained on specimens of alumina sintered at 1450 °C are shown.

[a] Semi-stable tests.

K_{IC} values determined for the fine grain sized alumina are inside the variability for crack-tip toughness, K_0, (1.5–3.0 MPa $m^{1/2}$) reported by Seidel and Rödel[40] and Fett et al.[41] for a series of aluminas with grain sizes in the range of 1–20 μm. These authors determined K_0 from "in situ" crack opening displacement (COD) measurements in a SEM and attributed the significant scatter of data to charging of the crack edges. Also, charging might lead to observed COD at the point of fracture and, consequently, calculated K_0 values, smaller than the real ones.

Apart from the experimental facts discussed above, differences between crack-tip toughness determined for different aluminas can be attributed to differences in fracture mode, as total toughness would be the sum of contributions of intergranular grain boundary fracture, cleavage across the easy fracture planes, and the increase in fracture surface due to deflection. A significant amount of transgranular fracture, independent from the grain size of the material, was reported by Seidel and Rödel[40] (20%), whereas only the largest grains (>5 μm) presented transgranular fracture in the fine-grained alumina studied here (Fig. 5a).

The classical linear fracture toughness parameters, K_{IC} and G_{IC}, are adequate to characterize fracture of the fine alumina, as revealed by the coincidence between J_{IC} and G_{IC} (Table 2), as occurs for perfectly linear materials.[28] On the contrary, the K_{IC} increase for the alumina with larger grain size was accompanied by J_{IC} being slightly higher than G_{IC}, revealing toughening. An increase in K_{IC} with grain size has been reported for other aluminas with similar microstructures.[35–36] However, coarse-grained materials with mean grain sizes larger than 10–20 μm, where intergranular fracture occurs for the largest grains (>50 μm) acting as bridges,[25,42–43] are required for significant toughening and rising *R*-curve behaviour.

There are no reported values of work of fracture for dense monophase alumina materials with a mean grain size lower than 5 μm. Even though the work of fracture values determined in the semi-stable tests reached in this work might be slightly overestimated, to the authors knowledge they are the lowest ever reported for dense fine-aluminas. For the alumina with the smallest average grain size (G_A = 3.5 μm, Table 1), the value determined in this work ($\gamma_{WOF} \cong 10$ J/m^2, Table 2) is higher than the value ($\gamma_f \cong 6$ J/m^2) reported by Wiederhorn for the rombohedral plane

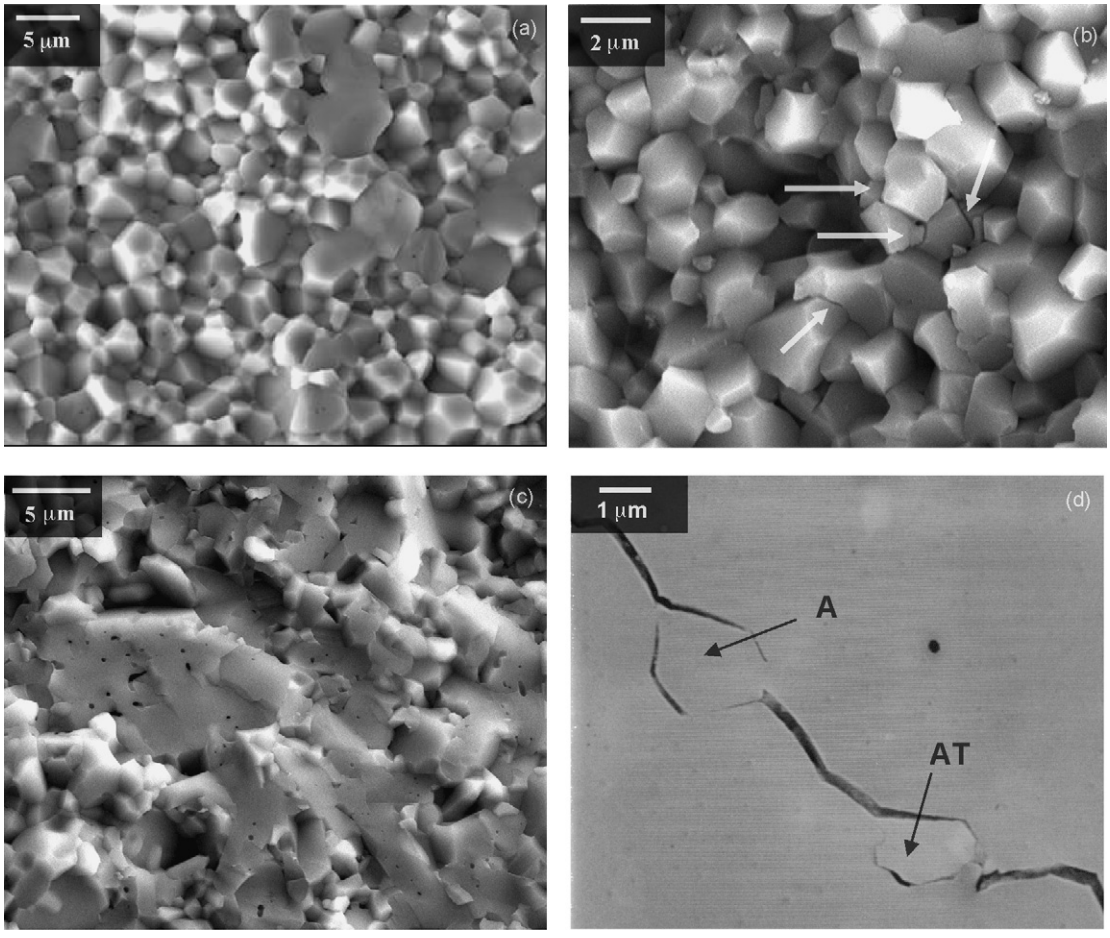

Fig. 5. Fractographic observations showing the mode of fracture of the materials. Scanning electron micrographs of fracture surfaces of SENVB specimens (a and b), strength specimens (c) and indentation cracks (d). (a) Monophase alumina sintered at 1450 °C. The largest grains (>5 μm) show transgranular fracture and the small ones show intergranular fracture. (b) Characteristic intergranular fracture in A10 composites with microcracks perpendicular to the fracture surfaces pointed by arrows. Specimen sintered at 1450 °C. (c) Mostly transgranular fracture in A10 composites previously obtained without no nanoparticles at grain boundaries (A10AT).[8] (d) Characteristic paths of indentation cracks in the A10 composites sintered at 1450 °C. Intact alumina (A) and aluminium titanate (AT) grains were observed along the crack trace.

which is the preferred cleavage plane in alumina monocrystals at room temperature.[44] The fracture energies generally determined for polycrystals are higher than those for monocrystals due to the contribution of intergranular fracture, in the same way as crack-tip toughness values in polycrystals are higher than those of the easy cleavage planes, as discussed above. Nevertheless, the coincidence between the values of $2\gamma_{WOF}$ and G_{IC} for this material (A-1450) would reveal the absence of significant crack-size dependent toughening phenomena.

For the coarser alumina ($G_A = 5.5\ \mu m$, Table 1), the work of fracture values ($\cong 20\ J/m^2$, Table 2) also coincide with those reported for aluminas with similar microstructures.[38] In this material, the fact that γ_{WOF} was slightly higher than G_{IC} reveals the action of limited additional energy consuming processes due to the interaction of the growing crack with the microstructure. Taking into account the materials properties and the stiffness of the testing device, the selected loading geometry and the specimen and crack sizes should lead to unstable crack growth for the four studied materials, according to Bar-On et al.[39] Nevertheless, semi-stable tests were obtained for the aluminas and were easier to obtain for A-1550 specimens than for the finer grained alumina. However, it was not possible to build the *R*-curve because it is not possible to calculate compliance at each unloading point for semi-unstable tests.

For the composites, the brittle fracture parameters, K_{IC} and G_{IC}, were similar, and higher than those corresponding to the alumina with similar grain size (A-1450, Table 2). On the contrary, the ratio J_{IC}/G_{IC} (Table 2) was slightly higher than 1 for the composite sintered at 1450 °C and increased for that fabricated at 1550 °C. Moreover, they presented rising *R*-curve behaviour (Fig. 6) with K_R increasing to the steady state value (K_∞) over a crack extension, Δa, of about 360 and 480 μm for A10-1550 and A10-1450, respectively. Therefore, the fracture behaviour of these materials would be more adequately described by the non-brittle fracture parameters, J_{IC} and *R* curve than by K_{IC} or G_{IC}. Extrapolation from the *R* curves (Fig. 6) showed crack-tip toughness, K_0, values similar for both composites and of the same order as that of the alumina material with similar grain size (A-1450, Table 2).

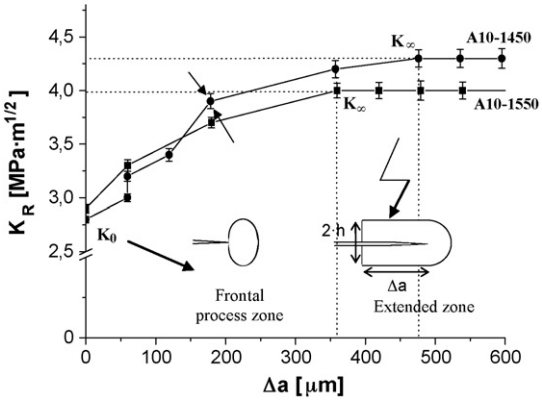

Fig. 6. Characteristic *R* curves determined for the composites from the load–displacement curves of notched specimens with a relative notch depth of 0.6 and considering the onset of crack propagation at the point where the non-linear behaviour starts in the load–displacement curves.

4.3. Toughening mechanisms in the composites

Toughness increase with crack extension ($\Delta K_R \cong 54\%$ and 38% for A10-1450 and A10-1550, respectively, Fig. 6) was observed for both composites. Moreover, they presented intergranular fracture (Fig. 5b), revealing the micrometric aluminium titanate grains located mainly at alumina triple points and grain boundaries, and numerous microcracks, perpendicular to the fracture surfaces, surrounding alumina and aluminium titanate grains. Microcracks were not observed at the polished surfaces and the materials presented reversible thermal expansion behaviour,[45,46] thus, the microcracks observed at the fracture surfaces should be formed during the fracture process. From the fracture surfaces of fine-grained materials it is not possible to ascertain whether such features are due to pull out of grains that have acted as bridges during the fracture process or actual microcracks developed during fracture.

Bridges are easily differentiated along the path of indentation cracks such as those shown in Fig. 5d in which relatively small grains of alumina (≅2–3 μm) and aluminium titanate (≅1–2 μm) that acted as frictional sliding bridges during fracture are observed. In general, crack bridging efficiency, in terms of ΔK_R and of the crack extension along which ΔK_R occurs, increases with bridge size.[4–5] Conversely, the smaller K_R increase and crack extension for the material with the largest grain sizes ($\Delta K_R \cong 1.1\ MPa\ m^{1/2}$ along a crack extension $\Delta a \cong 360\ \mu m$ and $\Delta K_R \cong 1.5\ MPa\ m^{1/2}$ along $\Delta a \cong 480\ \mu m$, for A10-1550 and A10-1450, respectively, Fig. 6) suggest that the main toughening mechanism was not bridging.

Post-fracture examinations of the zones that surrounded the notch and crack-tip regions in tested bend bars (Fig. 7) showed irregular shaped damaged zones (Fig. 7a) of widths ≅15–30 and 20–40 μm for the composites sintered at 1450 and 1550 °C, respectively. Detailed observations of these damaged zones revealed microcracking along grain boundaries (Fig. 7b). These observations demonstrate that microcracking acted as toughening mechanism during fracture of the composites. In general, microcracking is associated with low resistance of the materials to the propagation of small defects and, therefore, low strength values. Data in Table 1 clearly show how the composites developed here present significantly lower strength values than the one fabricated from already reacted aluminium titanate.[8] This material, in which no titanium segregation occurred at the alumina grain boundaries, presented mostly transgranular fracture and no microcracking, crack bridging being the only toughening mechanism observed.[8]

According to the microcracking model by Evans and Faber[47] and the work by Lutz et al.[48] it is possible to relate the width of the microcracked zones and the value of the crack-tip toughness, K_0, with the critical stress for microcrack initiation according to Eq. (6):

$$h = \frac{\sqrt{3}}{12\pi} \times (1+\nu)^2 \times \left(\frac{K_0}{\sigma_c}\right)^2 \quad (6)$$

where K_0 can be taken as the constant matrix crack-tip intensity factor, equal to K_{IC} for the monophase alumina with similar

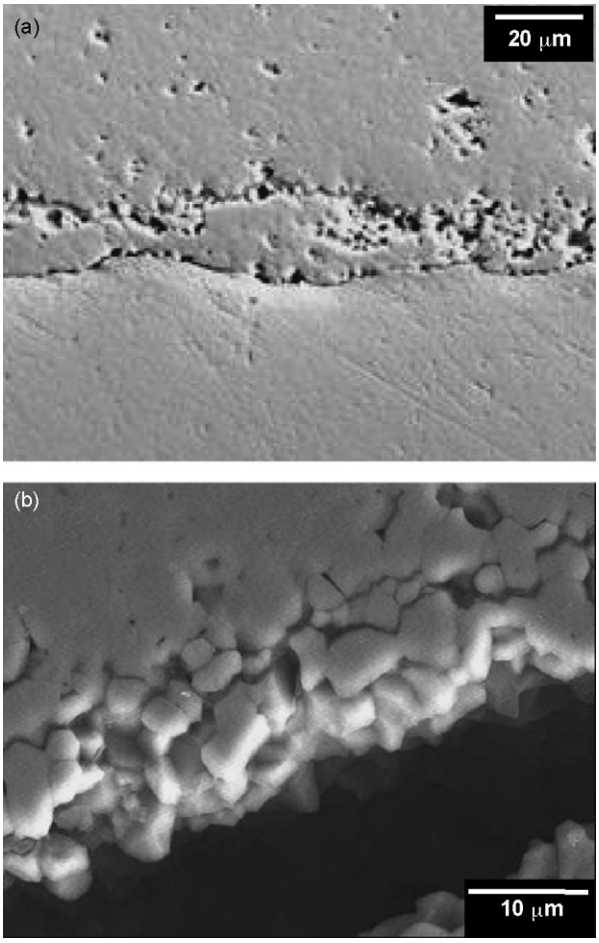

Fig. 7. Post-fracture observations of the zones that surrounded the notch and crack-tip region in the bend bars of A10. Scanning electron micrographs of polished and chemically etched (HF 10 vol.%–3 min) surfaces. (a) Damaged zone adjacent to one side of the crack (upper part of the image) in the composite sintered at 1450 °C. (b) Detail of microcracks in the composite sintered at 1550 °C.

grain size as those of the composites, A-1450. σ_c is the critical stress to trigger the microcracked process zone.

Inserting in Eq. (6) the average width values from Fig. 7 ($h \cong 20$ and 30 μm, for A10-1450 and A10-1550, respectively) and the K_0 values from Table 2 (2.8 MPa $m^{1/2}$), critical stresses (σ_c) of 163 and 133 MPa for A10-1450 and A10-1550, respectively, are obtained. These values are one order of magnitude higher than that determined by acoustic emission (20 MPa) for a coarse-grained (A123, 20–40 μm, $d_{50} = 16$ μm) alumina material[47,49] and for composite materials of zirconia–alumina in which significantly larger process zones ($h \cong$ mm) than the ones observed in the materials studied here were observed.[48] On the contrary, they are similar to those reported for zirconia–alumina composites with small microcrack process zones ($h \cong 60$–160 μm).[48] Even though the size of the process zone for the above mentioned coarse-grained alumina was not reported, its size should be larger than those observed in this work. In fact, using Eq. (6) and for K_0 the range of values determined by Seidel and Rödel[40] and Fett et al.[41]: 1.5–3 MPa $m^{1/2}$, process zones of $h = 384$–1539 μm are found.

Table 3
Values of G_{IC} in the R curves determined for the composites A10 with a relative notch depth of 0.6

	G_0 (S.D.) (J/m^2)	G_∞ (S.D.) (J/m^2)	J_{IC} (S.D.) (J/m^2)
A10-1450	21.4 (1.6)	58.5 (2.7)	45.9 (3.3)
A10-1550	29.4 (2.1)	56.9 (2.9)	53.1 (2.3)

G_0: initial values and G_∞: steady state values. The J_{IC} values correspond to Table 2. S.D.: standard deviation.

The different non-brittle mechanical parameters calculated in this work did not follow the same trend as a function of the microstructure of the composites. Toughness values from the R curves for completely developed process zones, K_∞ and G_∞ seem to be slightly higher for the fine-grained material, A10-1450, that presented smaller G_0 and process zone width, h, but significantly higher Δa across which the toughness increase (ΔK_R) occurred. On the contrary, J_{IC} was significantly higher for the coarse-grained composite, A10-1550, with larger G_0 and h and smaller Δa. This discrepancy is due to the fact that J_{IC} constitutes a fracture criterion for materials where the toughening occurs along limited crack propagation.[29] Therefore, J_{IC} will be closer to the toughness of composite A10-1550, for which the major part (76%) of the total toughness increase (38%) occurred along one half (180 μm) of the total crack growth before the steady state was reached (Fig. 6). On the contrary, significantly larger crack growth had to take place in the composite A10-1450 to reach the steady state. In this latter material, a crack growth of 230 μm occurred before the 76% of the total K_R increase (54%) was reached (Fig. 6).

The work of fracture values for the composites (Table 2) were considerably higher than those for the monophase aluminas in agreement with the toughening mechanisms described, and similar to those determined in dense alumina materials with a mean grain size of 25 μm ($\cong$50 J/m^2)[50] and in porous aluminas with a mean grain size of 15–20 μm ($\cong$40 J/m^2).[51] In those coarse-grained aluminas the main toughening mechanisms identified, crack bridging and crack branching,[52] were related to extensive grain boundary microcracking, at the expense of lower strength values ($\cong$300 MPa, 25% inferior to strength for fine-grained alumina).[53] The same drawback strength-microcracking occurs in the composites studied here, that present lower strengths than the previously studied composite material (28–36% lower, Table 1).

Moreover, work of fracture values substantially exceeded those of both energy–fracture toughness that resulted from the extension of the principles of linear elastic fracture to situations where the inelastic deformation occurs prior to fracture, J_{IC} and G_∞, ($\gamma_{WOF} > J_{IC}/2$, $G_\infty/2$, Tables 2 and 3). This fact suggests that there are additional non-linear phenomena occurring during fracture of the composites that significantly contribute to the total energy consumption but not to resistance to crack initiation and that can be envisaged as follows. The efficiency of microcraks in the toughening of the studied composites will be the result of a compromise between their crack shielding and weakening effects. For sufficient levels of microcrack density, microcracks could coalesce and link together with the crack front, leading to

a decrease of the fracture toughness of the material. Nevertheless, such microcracks could lead to the branching of the main crack and, consequently, to the increase of the fracture surface, leading to the increase of the total energy consumed during crack propagation. This second phenomenon would contribute to the resistance of the materials under loading conditions that imply high crack driving forces such as thermal shock.

5. Conclusions

Alumina + 10 vol.% aluminium titanate composites were obtained by reaction sintering of alumina and titania. The reaction sintering process promoted the formation of aluminium titanate nanometric grains at grain boundaries between the alumina grains.

This special microstructure led to extensive microcracking as the main toughening mechanism in the composites, which showed significant increments in work of fracture and flaw tolerance as compared with monophase alumina materials with similar microstructures.

The classical linear fracture toughness parameters, K_{IC} and G_{IC}, have demonstrated not to be adequate to characterize fracture of the composites, each fracture parameter analyzed, J_{IC}, R curve and work of fracture gave different information about the fracture behaviour of the material.

Acknowledgments

This work has been supported by the EC Human Potential Programme HPRN-CT-2002-00203, by the Project CICYT MAT2006-13480 (Spain) and the Postdoctoral Fellowship MEC EX-2006-0555 (Spain).

References

1. Harmer, M. P., Chan, H. M. and Miller, G. A., Unique opportunities for microstructural engineering with duplex and laminar ceramics composites. *J. Am. Ceram. Soc.*, 1992, **75**, 1715–1728.
2. Steinbrech, R. W., Toughening mechanisms for ceramic materials. *J. Eur. Ceram. Soc.*, 1992, **10**, 131–142.
3. Evans, A. G., Perspective on the development of high-toughness ceramics. *J. Am. Ceram. Soc.*, 1980, **73**, 187–206.
4. Lawn, B. R., Padture, N. P., Braun, L. M. and Bennison, S. J., Model for toughness curves in two-phase ceramics. I. Basic fracture mechanics. *J. Am. Ceram. Soc.*, 1993, **76**, 2235–2240.
5. Padture, N. P., Runyan, J. L., Bennison, S. J., Braun, L. M. and Lawn, B. R., Model for toughness curves in two-phase ceramics. II. Microstructural variables. *J. Am. Ceram. Soc.*, 1993, **76**, 2241–2247.
6. Padture, N. P., Bennison, S. J. and Chan, H. M., Flaw-tolerance and crack-resistance properties of alumina–aluminium titanate composites with tailored microstructures. *J. Am. Ceram. Soc.*, 1993, **76**, 2312–2320.
7. Runyan, J. L. and Bennison, S. J., Fabrication of flaw-tolerant aluminium-titanate-reinforced alumina. *J. Eur. Ceram. Soc.*, 1991, **7**, 93–99.
8. Uribe, R. and Baudin, C., Influence of a dispersion of aluminium titanate particles of controlled size on the thermal shock resistance of alumina. *J. Am. Ceram. Soc.*, 2003, **86**, 846–850.
9. Baudin, C., Sayir, A. and Berger, M. H., Mechanical behaviour of directionally solidified alumina/aluminium titanate ceramics. *Acta Mater.*, 2006, **54**, 3835–3841.
10. Bueno, S. and Baudin, C., Layered materials with high strength and flaw tolerance based on alumina and aluminium titanate. *J. Eur. Ceram. Soc.*, 2007, **27**, 1455–1462.
11. Dakskobler, A. and Kosmac, T., Preparation and properties of aluminium titanate–alumina composites. *J. Mat. Res.*, 2006, **21**, 448–454.
12. Manurung, P., Low, I. M. and O'Connor, B. H., Effect of beta-spodumene on the phase development in an alumina/aluminium-titanate system. *Mater. Res. Bull.*, 2005, **40**, 2047–2055.
13. Taylor, D., Thermal expansion data. XI. Complex oxides, A_2BO_5, and the garnets. *Br. Ceram. Trans. J.*, 1987, **86**, 1–6.
14. Taylor, D., Thermal expansion data. III. Sesquioxides, M_2O_3 with the corundum and the A-, B- and C-M_2O_3 structures. *Br. Ceram. Trans. J.*, 1984, **83**, 92–98.
15. Bueno, S., Moreno, R. and Baudin, C., Reaction sintered Al_2O_3/Al_2TiO_5 microcrack-free composites obtained by colloidal filtration. *J. Eur. Ceram. Soc.*, 2004, **24**, 2785–2791.
16. Guinea, G. V., Pastor, J. Y., Planas, J. and Elices, M., Stress intensity factor, compliance and CMOD for a general three-point-bend beam. *Int. J. Fract.*, 1998, **89**, 103–118.
17. Gogotsi, G. A., The use of brittleness measure (x) to represent mechanical behaviour of ceramics. *Ceram. Int.*, 1989, **15**, 127–129.
18. Sakai, M., Yoshimura, J., Goto, Y. and Inagaki, M., R-curve behaviour of a polycrystalline graphite: microcracking and grain bridging in the wake region. *J. Am. Ceram. Soc.*, 1988, **71**, 609–616.
19. Steinbrech, R. W., Reichl, A. and Schaarwächter, W. J., R-curve behaviour of long cracks in alumina. *J. Am. Ceram. Soc.*, 1990, **73**, 2009–2015.
20. Fett, T., Munz, D., Geraghty, R. D. and White, K. W., Influence of specimen geometry and relative crack size on the R-curve. *Eng. Fract. Mech.*, 2000, **66**, 375–386.
21. Wachtman, J. B., Stable crack propagation and R-curve behaviour. *Mechanical Properties of Ceramics*. John Willey & Sons Inc., New York, NY, 1996, pp. 141–157.
22. Fett, T. and Munz, D., Evaluation of R-curve effects in ceramics. *J. Mater. Sci.*, 1993, **28**, 742–752.
23. Hübner, H. and Jillek, W., Sub-critical crack extension and crack resistance in polycrystalline alumina. *J. Mater. Sci.*, 1977, **12**, 117–125.
24. Tanaka, K., Akiniwa, Y., Kimachi, H. and Kita, Y., R-curve behaviour in fracture of notched porous ceramics. *Eng. Fract. Mech.*, 2003, **70**, 1101–1113.
25. Ebrahimi, M. E., Chevalier, J. and Fantozzi, G., R-curve evaluation and bridging stress determination in alumina by compliance analysis. *J. Eur. Ceram. Soc.*, 2003, **23**, 943–949.
26. Hashida, T., Li, C. and Takahashi, H., New development of the J-based fracture testing technique for ceramic matrix composites. *J. Am. Ceram. Soc.*, 1994, **77**, 1553–1561.
27. Homeny, J., Darroudi, T. and Bradt, R. C., J-integral measurements of the fracture of 50% alumina refractories. *J. Am. Ceram. Soc.*, 1980, **63**, 326–331.
28. Rice, J. R., A path independent integral and the approximate analysis of strain concentration by notches and cracks. *J. Appl. Mech.*, 1968, **35**, 379–386.
29. Stevens, R. N. and Guiu, F., The application of the J-integral to problems of crack bridging. *Acta Metall. Mater.*, 1994, **42**, 1805–1810.
30. Droillard, C. and Lamon, J. J., Fracture toughness of 2-D woven SiC/SiC CVI-composites with multilayered interphases. *J. Am. Ceram. Soc.*, 1996, **79**, 849–858.
31. Bueno, S., Moreno, R. and Baudín, C., Design and processing of Al_2O_3-Al_2TiO_5 layered structures. *J. Eur. Ceram. Soc.*, 2005, **25**, 847–856.
32. Fullmann, R. L., Measurement of particle sizes in opaque bodies. *Trans. AIME, J. Met.*, 1953, **197**, 447.
33. Uribe, R. and Baudin, C., Aluminium titanate formation by solid-state reaction of alumina and titania. *Bol. Soc. Esp. Ceram. Vidr.*, 2000, **39**, 221–228.
34. Wieninger, H., Kromp, K. and Pabst, R. F., Crack resistance curves of alumina and zirconia at room temperature. *J. Mater. Sci.*, 1986, **21**, 411–418.
35. Rice, R. W., Freiman, S. W. and Becher, P. F., Grain-size dependence of fracture energy in ceramics. I. Experiment. *J. Am. Ceram. Soc.*, 1981, **64**, 345–350.

36. Mussler, B., Swain, M. V. and Claussen, N., Dependence of fracture toughness of alumina on grain size and test technique. *J. Am. Ceram. Soc.*, 1982, **65**, 566–572.
37. Damani, R., Gstrein, R. and Danzer, R., Critical notch-root radius effect in SENB-S fracture toughness testing. *J. Eur. Ceram. Soc.*, 1996, **16**, 695–702.
38. Sbaizero, O., Pezzotti, G. and Nishida, T., Fracture energy and R-curve behaviour of Al_2O_3/Mo composites. *Acta Mater.*, 1998, **46**, 681–687.
39. Bar-On, I., Baratta, F. I. and Cho, K., Crack Stability and its effect on fracture toughness of hot pressed silicon nitride beam specimens. *J. Am. Ceram. Soc.*, 1996, **79**, 2300–2308.
40. Seidel, J. and Rödel, J., Measurement of crack tip toughness in alumina as a function of grain size. *J. Am. Ceram. Soc.*, 1997, **80**, 433–438.
41. Fett, T., Munz, D., Sidel, J., Stech, M. and Rödel, J., Correlation between long and short crack R-curves in alumina using the crack opening displacement and fracture mechanical weight function approach. *J. Am. Ceram. Soc.*, 1996, **79**, 1189–1196.
42. Rödel, J., Kelly, J. F. and Lawn, B. R., In situ measurements of bridged crack interfaces in the scanning electron microscope. *J. Am. Ceram. Soc.*, 1990, **73**, 3313–3318.
43. Reichl, A. and Steinbrech, R. W., Determination of crack-bridging forces. *J. Am. Ceram. Soc.*, 1988, **71**, C-299–C-301.
44. Wiederhorn, S. M., Fracture of sapphire. *J. Am. Ceram. Soc.*, 1969, **52**, 485.
45. Bueno, S., Hernández, M. G., Sánchez, T., Anaya, J. J. and Baudin, C., Non destructive characterisation of alumina/aluminium titanate composites using a micromechanical model and ultrasonic determinations. Part I. Evaluation of the effective elastic constants of aluminium titanate. *Ceram. Int.*, 2008, **34**, 181–188.
46. Hernández, M. G., Bueno, S., Sánchez, T., Anaya, J. J. and Baudin, C., Non destructive characterisation of alumina/aluminium titanate composites using a micromechanical model and ultrasonic determinations. Part II. Evaluation of microcraking. *Ceram. Int.*, 2008, **34**, 189–195.
47. Evans, A. G. and Faber, K. T., Crack-growth resistance of microcracking brittle materials. *J. Am. Ceram. Soc.*, 1984, **67**, 255–260.
48. Lutz, E. H., Claussen, N. and Swain, M. V., K^R-curve behaviour of duplex ceramics. *J. Am. Ceram. Soc.*, 1991, **74**, 11–18.
49. Knehens, R. and Steinmbrech, R., Memory effect of crack resistance during slow crack growth in notched Al_2O_3 bend specimens. *J. Mater. Sci. Lett.*, 1982, **1**, 327–329.
50. Davidge, R. W. and Tappin, G., The effective surface energy of brittle materials. *J. Mater. Sci.*, 1968, **3**, 165–173.
51. Simpson, A., Effect of microstructure on measurements of fracture energy of Al_2O_3. *J. Am. Ceram. Soc.*, 1973, **56**, 7–11.
52. Wu, C. C. M., Freiman, S. W., Rice, R. W. and Mecholsky, J. J., Microstructural aspects of crack propagation in ceramics. *J. Mater. Sci.*, 1978, **13**, 2659–2670.
53. Chantikul, P., Bennison, S. J. and Lawn, B. R., Role of grain size in the strength and R-curve properties of alumina. *J. Am. Ceram. Soc.*, 1990, **73**, 2419–2427.